Available online at www.sciencedirect.com
ScienceDirect
Journal of Computational Physics 226 (2007) 836–851
JOURNAL OF COMPUTATIONAL PHYSICS
www.elsevier.com/locate/jcp

Roughness and cavitations effects on electro-osmotic flows in rough microchannels using the lattice Poisson–Boltzmann methods

Moran Wang [a,b,*], Jinku Wang [c], Shiyi Chen [a,d]

[a] Department of Mechanical Engineering, The Johns Hopkins University, 3400 N. Charles Street, Baltimore, MD 21218, United States
[b] Department of Biological and Agricultural Engineering, University of California, Davis, CA 95616, United States
[c] School of Aerospace, Tsinghua University, Beijing 100084, China
[d] College of Engineering and LTCS, Peking University, Beijing, China

Received 25 August 2006; received in revised form 26 March 2007; accepted 3 May 2007
Available online 22 May 2007

Abstract

This paper investigates the effects of roughness and cavitations in microchannels on the electro-osmotic flow behaviors using the Lattice Poisson–Boltzmann methods which combined one lattice evolution method for solving the non-linear Poisson–Boltzmann equation for electric potential distribution with the other lattice evolution method for solving the Navier–Stokes equations for fluid flow. The boundary conditions are correctly treated for consistency between the both. The results show that for the electro-osmotic flows in homogeneously charged rough channels, the flow rate does not vary with the roughness height or the interval space monotonically. The flow rate varies slightly with the roughness height or even increases a little when the roughness is very small, and then decreases when the roughness height is larger than 5% channel width. The flow rate decreases first and then increase with the roughness interval space. An interval space at twice roughness width makes the flow rate minimum. For the heterogeneously charged rough channel, the flow rate increases with the roughness surface potential at a super-linear rate. For the electro-osmotic flows in microchannels with cavitations, the flow rate change little with the cavitations depth when the depth value is very low and decreases sharply when the depth is greater than 3% channel width. The flow rate trends to be a constant when the cavitations are very deep. The flow rate decreases with the cavitations width but increases with the cavitations interval.

Keywords: Roughness and cavitation; Electro-osmotic flow; Lattice Poisson–Boltzmann method; Microfluidics

1. Introduction

With growing interests in bio-MEMS and bio-NEMS applications and fuel cell technologies, electrokinetic flows have become one of the most important non-mechanical techniques in microfluidics and nanofluidics

* Corresponding author. Address: Department of Mechanical Engineering, The Johns Hopkins University, 3400 N. Charles Street, Baltimore, MD 21218, United States. Tel.: +1 530 754 6770.
E-mail address: moralwang@jhu.edu (M. Wang).

0021-9991/$ - see front matter © 2007 Elsevier Inc. All rights reserved.
doi:10.1016/j.jcp.2007.05.001

[1–6]. Electro-osmotic flows (EOFs) have wide applications for pumping [7,8], separating [3] and mixing [9] in micro- and nanoscale devices. Due to their many applications, numerical simulations of EOF in micro- and nanochannels have recently received a great amount of attention [10–29]. The previous studies have mostly focused on smooth channels which, however, the realistic applications always go beyond. There are many roughness and cavitations on a real channel wall surface. To the authors' knowledge, only a little public literature concerns and presents full analyses of the EOFs in rough channels [16,17].

From the macroscopic point of view, the EOFs are governed by the Poisson–Boltzmann equation for electrical potential distributions and the Navier–Stokes equations for flows [10,13]. Accurate and efficient solution of the non-linear Poisson–Boltzmann equation is a challenge for both mathematicians and physicists. Up to now, hundreds of relative research papers appear every year on various scientific journals [30]. Most of previous researches have employed conventional PDE solvers, such as the finite difference method (FDM) and the finite element method (FEM) to solve the non-linear Poisson–Boltzmann equation in its linearized form [11–17]. Several researchers have also gained good predictions by solving the original non-linear Poisson–Boltzmann equation using FDM [18] or FEM [19], however with suffering from the huge computational costs from the strong non-linearity. The fast Fourier transform (FFT) [31] and the multi-grid [22,32] techniques greatly increase the efficiency of the numerical solution of the non-linear Poisson–Boltzmann equation; however they have seldom been extended for complex geometries.

In recent years, an efficient mesoscopic statistics-based method, the Lattice Boltzmann method (LBM), has been introduced into modeling the electrical potential distribution in confined domains [23–26,33–38]. Warren [33] introduced the "moment propagation" method to predict the electrical potential distribution for charged suspensions. He and Li [34] proposed a different scheme for analyzing the electrochemical processes in an electrolyte by using an independent lattice Boltzmann method to solve the Poisson equation for the ion diffusion. However, this method was based on a locally electrically neutral assumption so it was not suitable for analyzing the dynamics of charged suspensions [35]. Recently, Wang et al. [38] proposed a lattice evolution method by tracking the electric potential equation directly on discrete lattices for solving the non-linear Poisson–Boltzmann equation accurately and efficiently in confined domains. The method has been combined with the other lattice Boltzmann method, forming a lattice Poisson–Boltzmann method (LPBM), for applications of modeling the EOF in microchannels [24–26].

This paper focuses on the roughness and cavitations effects on EOFs in microchannels. To achieve the objects, the lattice Poisson–Boltzmann method will be developed for rough or cavitational channels. The consistency of boundary condition implements is correctly considered. The shape and arrangement effects of roughness or cavitations on the electro-osmotic flow behavior are therefore studied.

2. Numerical method

2.1. Evolution equation for electrical potential distribution

Electric double layer (EDL) theory [10] relates the electrostatic potential and the distribution of counterions and co-ions in the bulk solution by the Poisson equation as follows:

$$\nabla^2\psi = -\frac{\rho_e}{\varepsilon\varepsilon_0}, \tag{1}$$

where ψ is the electrical potential, ε the dimensionless dielectric constant of the solution, ε_0 the permittivity of a vacuum and ρ_e the net charge density. According to classical EDL theory, the equilibrium Boltzmann distribution equation can be used to describe the ionic number concentration for dilute small-ion solutions. Therefore, the net charge density distribution can be expressed as the sum of all the ions in the solution

$$\rho_e = \sum_i z_i e n_{i,\infty} \exp\left(-\frac{z_i e}{k_b T}\psi\right), \tag{2}$$

where the subscript i represents the ith species, n_∞ is the bulk ionic number concentration, z the valence of the ions (including the sign), e the absolute value of one proton charge, k_b the Boltzmann constant and T the absolute temperature.

Substituting Eq. (2) into Eq. (1) yields the non-linear Poisson–Boltzmann equation for the electrical potential in the dilute electrolyte solution

$$\nabla^2\psi = -\frac{1}{\varepsilon\varepsilon_0}\sum_i z_i e n_{i,\infty}\exp\left(-\frac{z_i e}{k_b T}\psi\right). \tag{3}$$

Eq. (3) can be solved using 1D or 2D linearized simplifications [20,21], iteration [11,12] or multi-grid methods [22,32]. Hirabayashi et al. [36,37] ever developed a lattice Bhatnagar-Gross-Krook (BGK) model for the Poisson equation where, however, the source term was limited to a linear term or a fluctuation near zero. The model was hardly used to solve a non-linear Poisson–Boltzmann equation. Here we use the lattice Poisson method for the non-linear Poisson–Boltzmann equation in confined domains [38] to solve Eq. (3).

The solution of Eq. (3) can be regarded as the steady solution of

$$\frac{\partial\psi}{\partial t} = \nabla^2\psi + g_{\mathrm{rhs}}(\mathbf{r},\psi,t), \tag{4}$$

where $g_{\mathrm{rhs}} = \frac{1}{\varepsilon\varepsilon_0}\sum_i z_i e n_{i,\infty}\exp(-\frac{z_i e}{k_b T}\psi)$ represents the negative term of right hand side (RHS) of Eq. (3).

The evolution equation for the electrical potential on the two-dimensional night-directional (D2Q9) discrete square lattices can then be written as [38].

$$g_\alpha(\mathbf{r}+\Delta\mathbf{r}, t+\delta_{t,g}) - g_\alpha(\mathbf{r},t) = -\frac{1}{\tau_g}[g_\alpha(\mathbf{r},t) - g_\alpha^{\mathrm{eq}}(\mathbf{r},t)] + \left(1-\frac{0.5}{\tau_g}\right)\delta_{t,g}\omega_\alpha g_{\mathrm{rhs}}, \tag{5}$$

where $\mathbf{r}$ is the position vector, $\delta_{t,g}$ the time step, τ_g the dimensionless relaxation time, g^{eq} the equilibrium distribution of evolution variable g:

$$g_\alpha^{\mathrm{eq}} = \varpi_\alpha\psi \quad \text{with } \varpi_\alpha = \begin{cases} 0 & \alpha = 0 \\ 1/6 & \alpha = 1,2,3,4 \\ 1/12 & \alpha = 5,6,7,8 \end{cases} \tag{6}$$

and

$$\omega_\alpha = \begin{cases} 4/9 & \alpha = 0 \\ 1/9 & \alpha = 1,2,3,4\,. \\ 1/36 & \alpha = 5,6,7,8 \end{cases} \tag{7}$$

The time step

$$\delta_{t,g} = \delta_x/c', \tag{8}$$

where δ_x is the lattice constant and c' is a *pseudo* sound speed in the potential field whose value can be artificial to vary the time step [38]. The dimensionless relaxation time

$$\tau_g = \frac{3\chi\delta_{t,g}}{2\delta_x^2} + 0.5, \tag{9}$$

where χ is defined as the potential diffusivity which is equal to unity in the simulations.

The evolution Eqs. (5)–(9) can be proved consistent with the macroscopic non-linear Poisson–Boltzmann equation, Eq. (4). After evolving on the discrete lattices, the macroscopic electrical potential can be calculated using

$$\psi = \sum_\alpha (g_\alpha + 0.5\delta_{t,g} g_{\mathrm{rhs}}\omega_\alpha). \tag{10}$$

Though the electrical potential evolution equations are in an un-steady form, only the steady state result is realistic, because the electromagnetic susceptibility has not been considered. Although the lattice evolution method for non-linear Poisson equation is not as efficient as the multi-grid solutions due to its long wavelength limit, it has the advantages of suitability for complex geometries and parallel computing. Although this paper only presents 2D cases, the algorithm is easy to extend to a 3D case.

2.2. Evolution equation for fluids with external forces

For the flows with external forces, the continuous Boltzmann–BGK equation with an external force term, F, is [39–41]

$$\frac{\mathrm{D}f}{\mathrm{D}t} \equiv \partial_t f + (\boldsymbol{\xi}\cdot\nabla)f = -\frac{f-f^{\mathrm{eq}}}{\tau} + F, \tag{11}$$

where $f \equiv f(x,\boldsymbol{\xi},t)$ is the single particle distribution function in the phase space $(x,\boldsymbol{\xi})$, $\boldsymbol{\xi}$ the microscopic velocity, τ the relaxation time and f^{eq} the Maxwell–Boltzmann equilibrium distribution. For a steady fluid immersed in a conservative force field, the equilibrium distribution function is defined by adding a Boltzmann factor to the Maxwell–Boltzmann distribution

$$f^{\mathrm{eq}} = \frac{\rho_0}{(2\pi RT)^{D/2}}\exp\left(-\frac{U}{k_{\mathrm{b}}T}\right)\exp\left(-\frac{(\boldsymbol{\xi}-\mathbf{u})^2}{2RT}\right), \tag{12}$$

where U is the potential energy of the conservative force field, ρ_0 the fluid density where U is lowest, R the ideal gas constant, D the dimension of the calculation space(1D, 2D or 3D) and $\mathbf{u}$ the macroscopic velocity. Here the external force term, F, needs to be chosen carefully. Dimensional analysis led to the following form of F:

$$F = \frac{\mathbf{G}\cdot(\boldsymbol{\xi}-\mathbf{u})}{RT}f^{\mathrm{eq}}, \tag{13}$$

with $\mathbf{G}$ being the external force per unit mass [42]. Eq. (3) has a perfect accuracy (relative errors are less than 0.5% when comparing with analytical solutions for a Poiseuille flow), even though ones reported it was an only first order approximation [43].

The Chapman–Enskog expansion can be used to transform the Boltzmann–BGK equation, Eq. (11), into the correct continuum Navier–Stokes equations,

$$\rho\frac{\partial\mathbf{u}}{\partial t} + \rho\mathbf{u}\cdot\nabla\mathbf{u} = -\nabla P + \mu\nabla^2\mathbf{u} + \mathbf{F}_E, \tag{14}$$

where ρ is the solution density, P the pressure, μ the dynamic fluid viscosity and $\mathbf{F}_E$ the electric force density vector. In general, the electrical body force in electrokinetic fluids can be expressed as

$$\mathbf{F}_E = \mathbf{F}_{\mathrm{ext}} + \rho_e(\mathbf{E}_{\mathrm{int}} + \boldsymbol{\xi}\times\mathbf{B}_{\mathrm{int}}) + \mathbf{F}_V, \tag{15}$$

where $\mathbf{F}_{\mathrm{ext}}$ represents the external field body forces, including the Lorentz force associated with any externally applied electric and magnetic field. For only an electrical field, $\mathbf{F}_{\mathrm{ext}} = \rho_e\mathbf{E}$, where $\mathbf{E}$ is the electrical field strength. $\mathbf{E}_{\mathrm{int}}$ and $\mathbf{B}_{\mathrm{int}}$ are internally smoothed electrical and magnetic fields due to the motion of the charged particles inside the fluid. $\mathbf{F}_V$ is a single equivalent force density due to the intermolecular attraction [20].

The two-dimensional nine-speed (D2Q9) lattice Boltzmann model gives the evolution equation of the discrete density distribution [39]

$$f_\alpha(\mathbf{r}+\mathbf{e}_\alpha\delta_t, t+\delta_t) - f_\alpha(\mathbf{r},t) = -\frac{1}{\tau_v}[f_\alpha(\mathbf{r},t) - f_\alpha^{\mathrm{eq}}(\mathbf{r},t)] + \delta_t F_\alpha, \tag{16}$$

where $\mathbf{e}_\alpha$ is the discrete velocities

$$\mathbf{e}_\alpha = \begin{cases} (0,0) & \alpha = 0 \\ (\cos\theta_\alpha, \sin\theta_\alpha)c, \theta_\alpha = (\alpha-1)\pi/2 & \alpha = 1-4 \\ \sqrt{2}(\cos\theta_\alpha, \sin\theta_\alpha)c, \theta_\alpha = (\alpha-5)\pi/2+\pi/4 & \alpha = 5-8 \end{cases}, \tag{17}$$

f_α^{eq} the equilibrium distribution

$$f_\alpha^{\mathrm{eq}} = \omega_\alpha\rho_0\exp\left(-\frac{U}{k_{\mathrm{b}}T}\right)\left[1 + 3\frac{\mathbf{e}_\alpha\cdot\mathbf{u}}{c^2} + 9\frac{(\mathbf{e}_\alpha\cdot\mathbf{u})^2}{c^4} - \frac{3\mathbf{u}^2}{2c^2}\right], \tag{18}$$

δ_t the time step and τ_v the dimensionless relaxation time. The external force term is [25]

$$F_\alpha = \frac{\mathbf{G}\cdot(\mathbf{e}_\alpha - \mathbf{u})}{RT} f_\alpha^{\mathrm{eq}}(\mathbf{r}, t). \tag{19}$$

The macroscopic density and velocity can be calculated using

$$\rho = \sum_\alpha f_\alpha, \tag{20}$$

$$\rho\mathbf{u} = \sum_\alpha \mathbf{e}_\alpha f_\alpha. \tag{21}$$

The dimensionless relaxation time, τ_v, is a function of the fluid viscosity

$$\tau_v = 3v\frac{\delta_t}{\delta_x^2} + 0.5, \tag{22}$$

where v is the kinetic viscosity.

For electrokinetic flows in dilute electrolyte solutions, the external electrical force in Eq. (15) can be simplified to:

$$\mathbf{F}_E = \rho_e\mathbf{E} - \rho_e\nabla\Phi, \tag{23}$$

where Φ is the stream electrical potential caused by the ion movements in the solution based on the Nernst–Planck theory. Generally, the stream potential dominates the electro-viscosity effect in pressure driven flows, but its value is much less than the external potential and can be ignored in electrically driven flows. Therefore, the external force in the discrete Lattice Boltzmann equation (Eq. 18) should include the pressure and electric force

$$F_\alpha = \frac{(-\nabla P + \rho_e\mathbf{E} - \rho_e\nabla\Phi)\cdot(\mathbf{e}_\alpha - \mathbf{u})}{\rho RT} f_\alpha^{\mathrm{eq}}. \tag{24}$$

Eqs. (16)–(24) can then be solved to analyze electrokinetic flows using the LBM as long as the charge density distribution in the solution is known.

2.3. Boundary conditions

For the evolution equation of the electrical potential, we used a second-order accurate Dirichlet boundary condition implement on the wall surfaces and the periodic conditions were implemented at both inlet and outlet.

For the Dirichlet boundary, the unknown distribution functions at the boundary were assumed to be equilibrium distribution functions with a counter-slip internal energy density with the source, g_{rhs} [44]. For example, for a straight upper wall, g_4, g_7 and g_8 are unknown, but can be obtained from the equilibrium distribution of the local ψ_0:

$$\psi_0 = 3\psi_{\mathrm{s}} - 3S_{\mathrm{p}} - 1.5\delta_t\sum_\alpha \omega_\alpha g_{\mathrm{rhs}}, \tag{25}$$

where S_{p} is the sum of known populations coming from the internal nodes and nearest wall nodes

$$S_{\mathrm{p}} = g_0 + g_1 + g_2 + g_3 + g_5 + g_6, \tag{26}$$

and ψ_{s} is the boundary value. Thus the unknown distributions are

$$g_\alpha = \varpi_\alpha\psi_0. \tag{27}$$

Convex and concave corners exist in roughness and cavitations. They can be treated in a similar way. The upper-right convex corner, for example, has five unknown populations g_1, g_2, g_5, g_6 and g_8. They also follow from Eq. (25) with

$$\psi_0 = \frac{12\psi_{\mathrm{s}} - 6\delta_t\sum_\alpha \omega_\alpha g_{\mathrm{rhs}} - 12S_{\mathrm{p}}}{7}, \tag{28}$$

where the known populations g_3, g_4 and g_7 lead to

$$S_p = g_0 + g_3 + g_4 + g_7. \tag{29}$$

Therefore the unknown distributions are determined by Eq. (27).

The lower-left concave corner, for example, has only one unknown population g_5 which can be calculated by

$$\psi_0 = 12\psi_s - 6\delta_t \sum_\alpha \omega_\alpha g_{rhs} - 12S_p, \tag{30}$$

where

$$S_p = g_0 + g_1 + g_2 + g_3 + g_4 + g_6 + g_7 + g_8, \tag{31}$$

and therefore the unknown population is

$$g_5 = \psi_0/12. \tag{32}$$

For the evolution for fluid flow, the conventional bounce-back model was mostly used in previous works. Although this model is easy to deal with the complex geometries, a detail study has shown it has half a lattice displacement on the boundary [45,46]. To treat the boundary conditions consistent between the electric potential and fluid flow evolutions, a non-slip model is used here to model the fluid-solid interaction on the wall surfaces [47].

For still walls, the unknown density distribution functions at the wall are calculated from the local equilibrium distribution function with a counter slip velocity. For example, for a straight upper wall, f_4, f_7 and f_8 are unknown, and can be obtained from an equilibrium distribution function with a counter slip velocity

$$u' = 6\frac{-(f_1 - f_3 + f_5 - f_6)}{\rho'}c, \tag{33}$$

where

$$\rho' = 6(f_2 + f_5 + f_6). \tag{34}$$

Thus the unknown density distributions are

$$f_\alpha = \omega_\alpha \rho' \left[1 + 3\frac{u'}{c} + 9\frac{(u')^2}{c^2} - \frac{3(u')^2}{2c^2}\right]. \tag{35}$$

For the cases at both convex and concave type corners, it is hard to determine the counter-slip velocities. Here we simplify the unknown populations determined by the equilibrium distributions at zero counter-slip velocities. Periodic conditions are implemented at inlet and outlet.

3. Results and discussion

The lattice Poisson–Boltzmann method is applied to simulate the EOF in 2D microchannels by two steps: firstly the lattice Poisson method solves the non-linear Poisson–Boltzmann equation for a stable electrical potential distribution; secondly the lattice Boltzmann method is used to simulate the steady electrically-driven fluid flow in the microchannel. This section shows the effects of boundary implement consistency on the EOF in straight smooth channels at first, and then analyzes the effects of roughness and cavitations in rough microchannels on the EOF characteristics with different shapes and arrangements considered.

The accuracy of the present lattice Poisson–Boltzmann method lies on the lattice size relative to the width of electric double layer. Previous study showed the lattice size should be smaller than the EDL width for an accurate numerical simulation [38]. In the simulations of this work, we keep the lattice size much smaller than the EDL width, i.e. δ_x is usually 1/10 to 1/3 each EDL width. We initialize a still system and judge the steady status of electrical potential and velocity distributions by relative errors every 100 steps at the middle point are smaller than 10^{-10}. The computational efficiency depends also on the chosen dimensionless relaxation times (τ). Well-chosen values of the relaxation times would make each simulation cost minutes to hours on a 2.0G CPU depending on the grid number.

3.1. Straight smooth channel cases

The electrically-driven osmotic flows in a straight homogeneously charged channel are simulated using the consistent lattice evolution methods. We change the external electrical field strength, the wall surface zeta potential, the bulk ionic molar concentration and the channel width. It is found that the bulk velocity is nearly proportional to the external electrical field strength, as well as the surface zeta potential, which agree well with the previous experimental data [48], numerical results [21], and even recent MD simulations in nanochannel flows [49,50].

Fig. 1 shows the velocity profiles for the various bulk ionic concentrations c_∞. The channel width is 0.4 μm, the external electric field strength $E = 5 \times 10^2$ V/m and the surface zeta potential $\psi_s = -50$ mV for both walls. The fluid properties are set as those of water at the standard state which are the dielectric constant $\varepsilon\varepsilon_0 = 6.95 \times 10^{-10}$ C^2/J m, the density $\rho = 1.0 \times 10^3$ kg/m^3 and the viscosity $\mu = 0.89$ Pa s. The results show an optimal ionic concentration that maximizes average velocity. As the ionic molar concentration decreases from a high value (2×10^{-2}), the EDL thickness increases so that although the force is slightly reduced, the electrical force domain increases and thus the average velocity increases. There exists a concentration at which the effect of the electrical force can dominate across the entire channel and make the velocity reach maximum (10^{-4} to 10^{-3} M for current simulations). As the ionic concentration decreasing (such as from 10^{-4} to 10^{-6}), the force reduction becomes the most important factor and the average velocity decrease. The lower ionic concentrations also result in a more parabolic-like velocity profile. These results are similar as those in Ref. [24] qualitatively, however different quantitatively at high ionic concentrations. The reason lies in the boundary implement inconsistency between the two evolution methods in the previous research [24].

Fig. 2 shows the velocity profiles for various channel widths for $c_\infty = 10^{-4}$ M, $E = 5 \times 10^2$ V/m and $\psi_s = -50$ mV. The channel width varies from 0.1 μm to 1 μm. Totally different from the previous results [24], the average velocity shows good monotonicity with the channel width. For channel widths larger

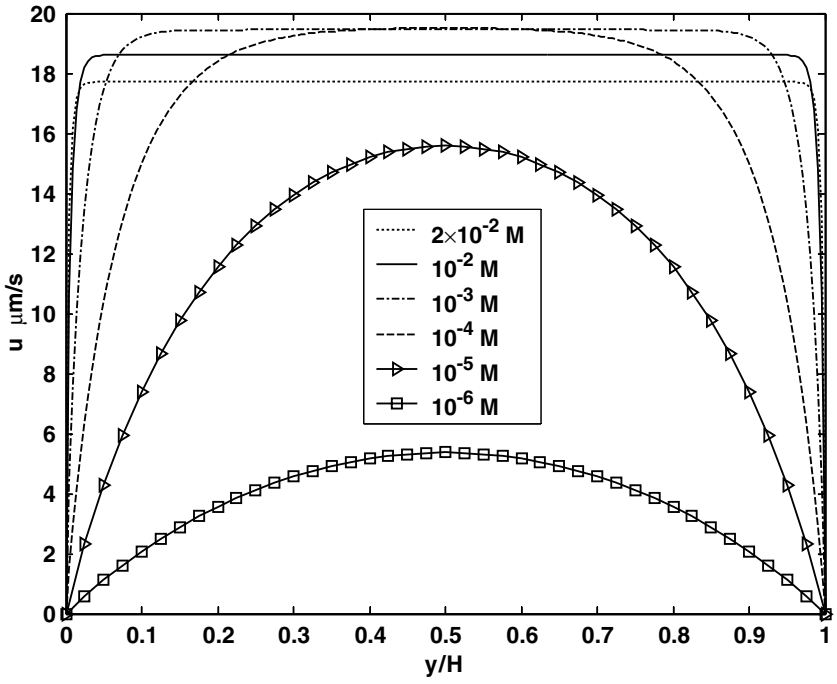

Fig. 1. Velocity profiles for various ionic molar concentrations for electrically driven flow. The dotted line: $c_\infty = 2 \times 10^{-2}$ M; the solid line: $c_\infty = 10^{-2}$ M; the dash-dot line: $c_\infty = 10^{-3}$ M; the dashed line: $c_\infty = 10^{-4}$ M; the triangle-line: $c_\infty = 10^{-5}$ M; the square-line: $c_\infty = 10^{-6}$ M.

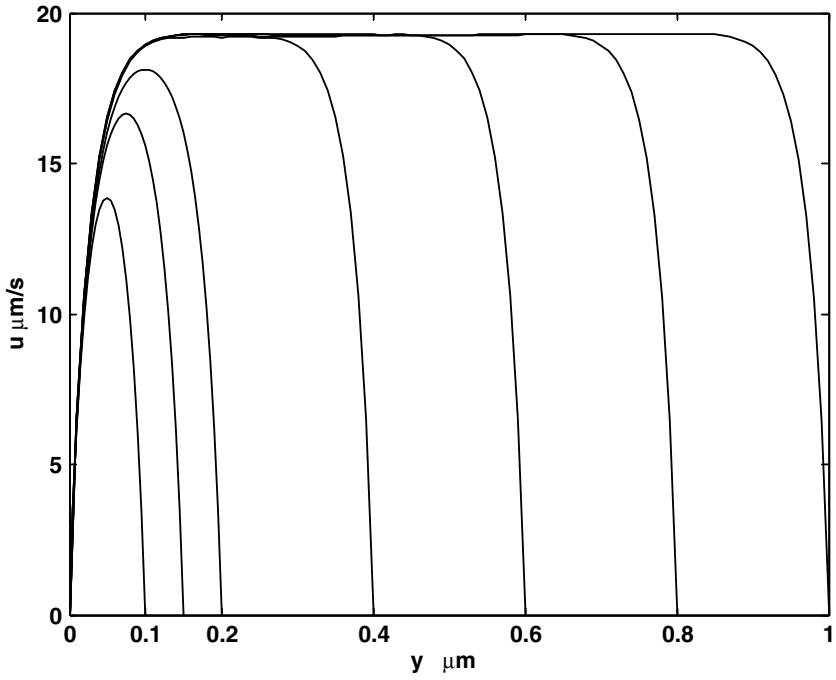

Fig. 2. Velocity profiles for different channel widths with $c_\infty = 10^{-4}$ M, $E = 5 \times 10^2$ V/m and $\psi_s = -50$ mV.

than double size of the EDL thickness, the maximum velocity seldom changes with the channel width. However, for channels widths less than double size of the EDL thickness, a smaller channel width leads to a smaller velocity. Similar results can be found in the previous simulations under the linearization assumption [21].

3.2. Roughness effects

The roughness is simplified as a group of rectangles on the lower channel wall here, as shown in Fig. 3. The channel is H in width, with both wall charged with a surface potential ψ_s. The channel is periodic in x direction. The roughness is w in width and h in height. The roughness is uniformly arranged in the channel with an interval space D. The three surfaces of each roughness are charged at a surface potential ψ_r. The A–A section is the middle cross section for each roughness. The electrolyte solution is driven by an external electrical field E. The fluid parameters are same as used in Section 3.1. Here we consider various cases for different roughness heights (h), different arrangement interval spaces (D) and different surface potentials (ψ_r).

Fig. 4 shows the velocity profiles at A–A section for different roughness heights. The ionic concentration of the electrolyte solution is $c_\infty = 10^{-4}$ M. The external electrical field strength is $E = 5 \times 10^2$ V/m. Both the channel and roughness surfaces are homogeneously charged at $\psi_s = \psi_r = -50$ mV. The channel width is 0.4 μm and divided into 40 lattices. The roughness width is $w = H/4$ and the interval space $D = 3H/4$. The roughness height h changes from 0 (smooth case) to $H/4$. The results show that the velocity maximum increases with the roughness height, and the velocity profile becomes asymmetric. The reason is that the roughness does not only change the channel cross section area, but also change the potential distribution and therefore the electric driving force on the fluid. Thus there are two factors actually influencing the flow rate through the channel. Fig. 5 shows the flow rate changing with the roughness height. The results indicate that the electrically-driven flow rate changes very slowly with the roughness height when the roughness is very small ($h/H < 0.05$). A very short roughness ($h/H < 0.025$) seems even enhancing the flow rate a little bit. The charged roughness plays two roles: first it changes the electrical field distribution which may enhance the elec-

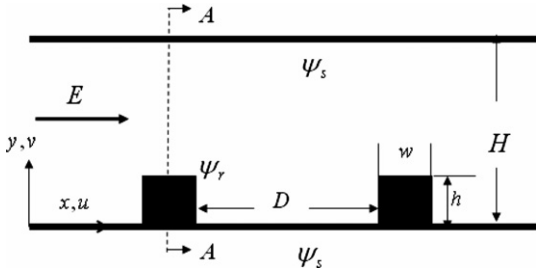

Fig. 3. Geometries and boundary conditions for the microchannel with roughness.

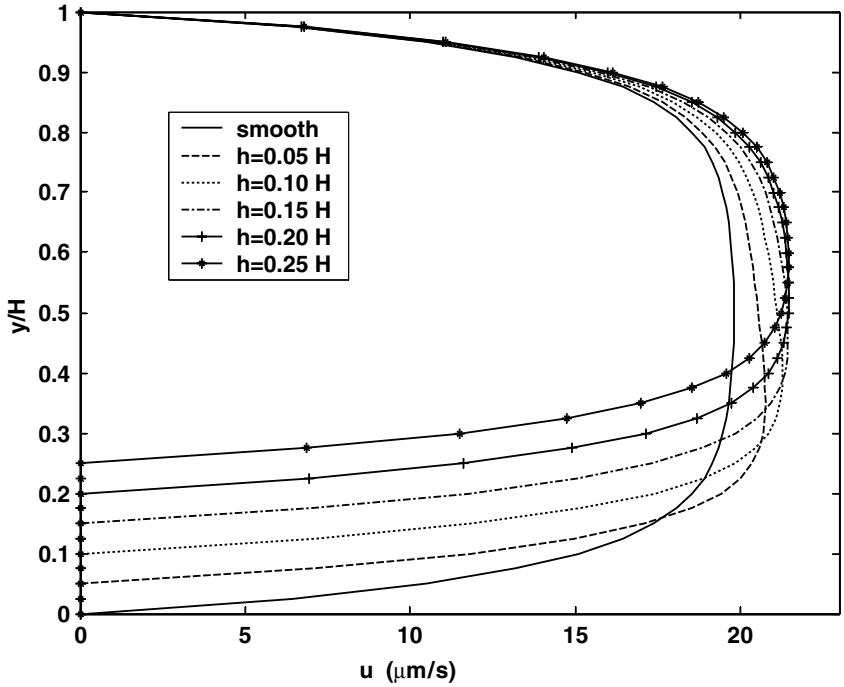

Fig. 4. Velocity profiles at A-A section for different roughness heights with $c_\infty = 10^{-4}$ M, $E = 5 \times 10^2$ V/m, $\psi_s = \psi_r = -50$ mV, $H = 0.4$ μm, $w = H/4$ and $D = 3H/4$.

tric driving force, and second it also increase the flow resistance. When the former factor dominates, the flow rate could increase; otherwise the flow rate will decrease. When the roughness height is larger than 1/10 channel width, the flow rate will decrease sharply with the roughness height. The interesting anomalous variation of flow rate with the roughness height has not been reported and validated in the previous work. A further analysis and consideration on the flow mechanism will be performed in the future work using our multi-scale simulation tools by coupling atomistic and continuum methods.

Fig. 6 shows the flow rates influenced by the roughness interval space when both the roughness width and height are at $H/4$. The other parameters are $c_\infty = 10^{-4}$ M, $E = 5 \times 10^2$ V/m, $\psi_s = \psi_r = -50$ mV and $H = 0.4$ μm. When the roughness interval is smaller than twice the roughness width, the flow rate decrease with the interval space; however, when the roughness interval is larger than twice the roughness width, a larger interval space leads to a larger flow rate. It is noticed that even for very sparse roughness cases, such as $D = 15w$, the flow rate is lower than 90% that of a smooth channel, which shows that the roughness effect is not negligible in analysis of electro-osmotic flows in microfluidics.

The heterogeneously charged rough channel is also simulated here. We remain the channel surface potential $\psi_s = -50$ mV and change the roughness surface potential ψ_r from -10 to -120 mV. The asymmetric potential

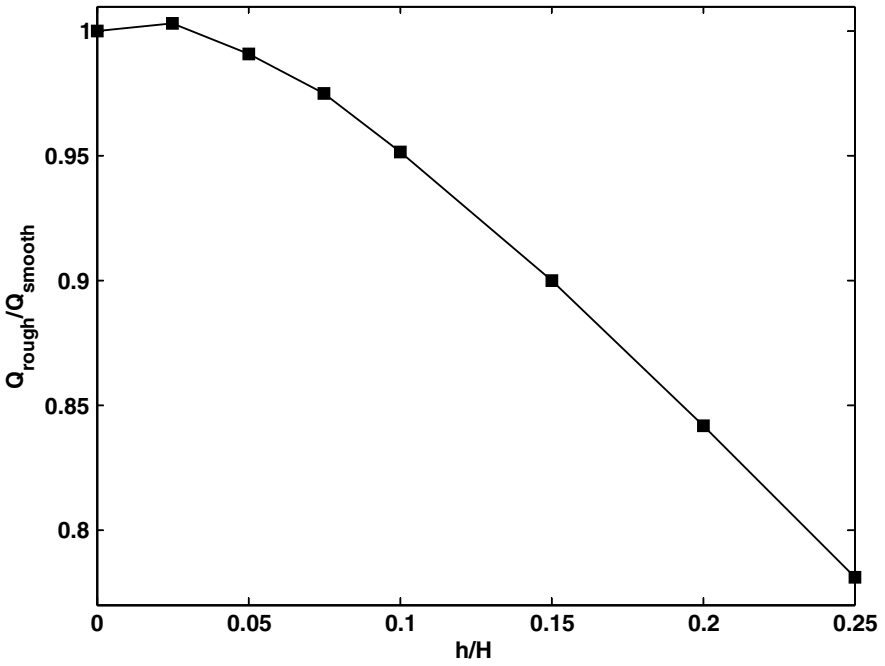

Fig. 5. Flow rate variation with the roughness height with $c_\infty = 10^{-4}$ M, $E = 5 \times 10^2$ V/m, $\psi_s = \psi_r = -50$ mV, $H = 0.4$ μm, $w = H/4$ and $D = 3H/4$.

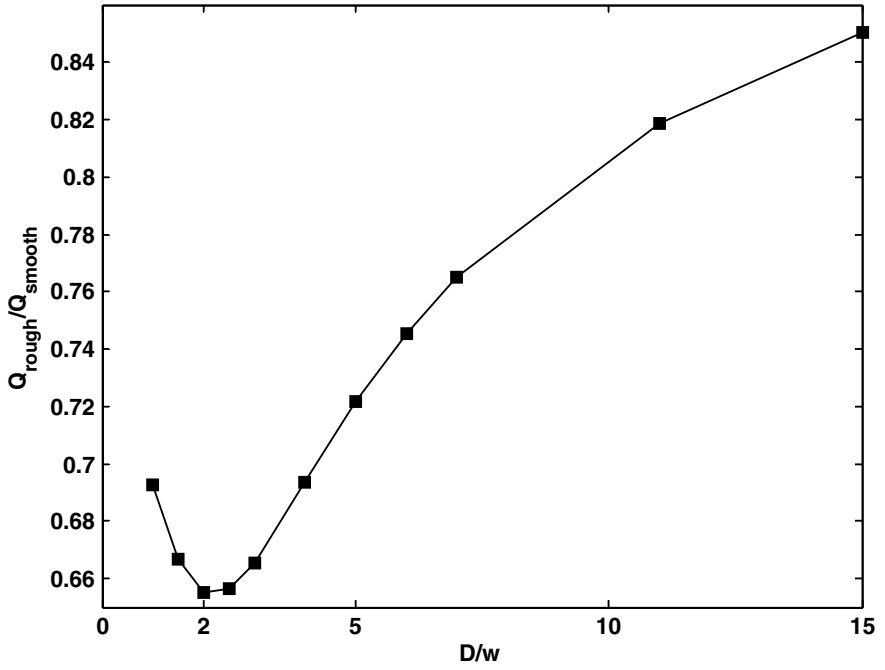

Fig. 6. Flow rate variation with the roughness interval space with $c_\infty = 10^{-4}$ M, $E = 5 \times 10^2$ V/m, $\psi_s = \psi_r = -50$ mV, $H = 0.4$ μm, $w = H/4$ and $h = H/4$.

boundaries destroy the flow symmetry, as shown in Fig. 7a. Larger values of the surface potential induce larger velocities near the surface. The flow rate also increases with the roughness surface potential superlinearly, shown as Fig. 7b. For the current case, when the roughness surface potential is −120 mV, the flow rate of the

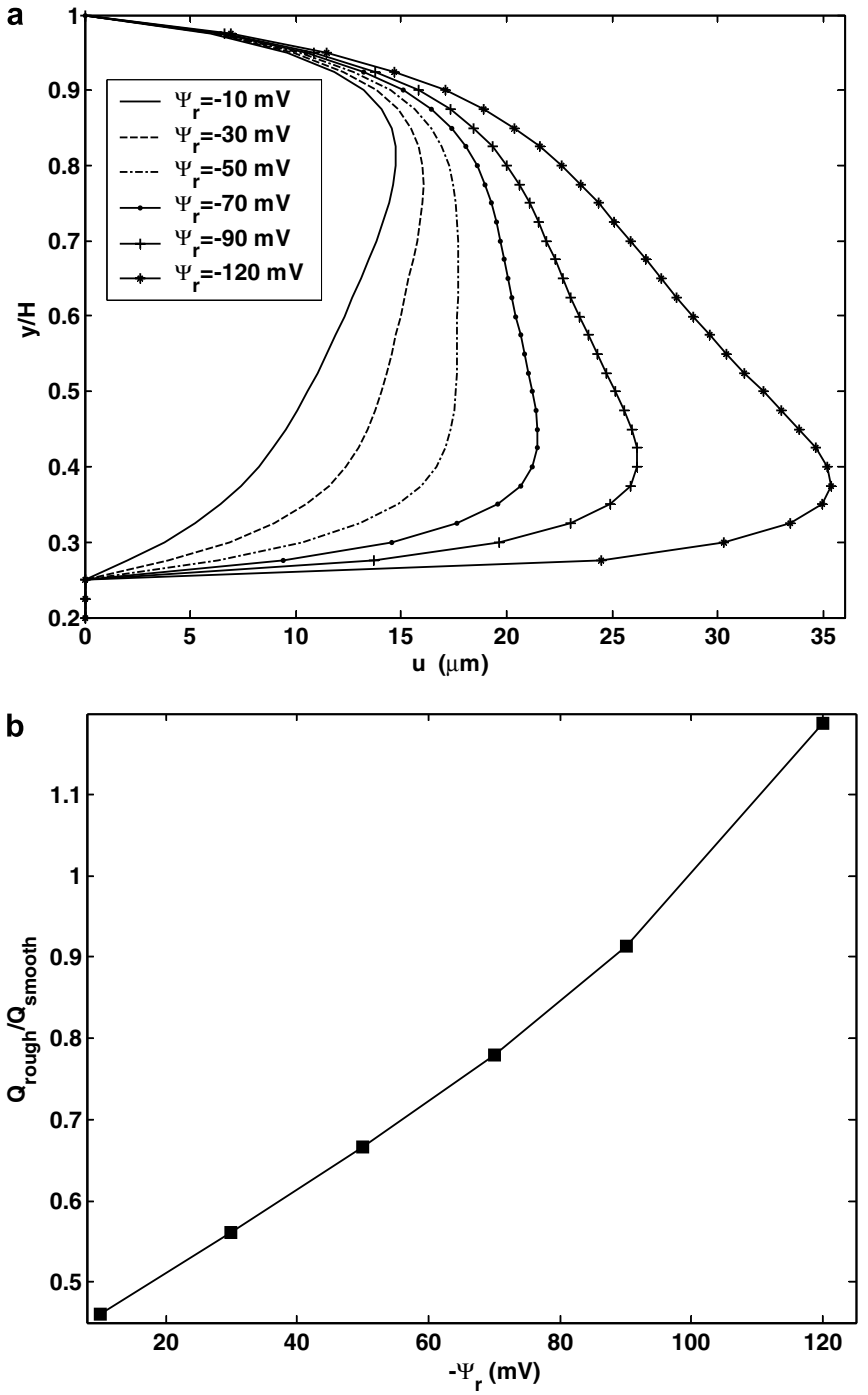

Fig. 7. Heterogeneously charged roughness cases where $c_\infty = 10^{-4}$ M, $E = 5 \times 10^2$ V/m, $\psi_s = -50$ mV, $H = 0.4$ μm, $w = H/4$, $D = 3H/4$ and $h = H/4$. (a) Velocity profiles at A–A section (b) flow rate varies with the roughness surface potential.

rough channel is even higher than that of the homogeneously charged smooth channel. Such characteristics could be used to enhance the flow rate in microfluidics by inserting high-surface-potential objects into the microchannel.

3.3. Cavitations effects

Both roughness and cavitations are fundamental elements on a rough channel surface. In macroscopic flow, no divisions have been made between them. However, in micro channel flow, some difference has been reported on the flow friction between roughness and cavitations [51,52]. Here we simulate the electro-osmotic flows in microchannels with cavitations, which has been seldom studied before.

The concerned microchannel with cavitations is shown in Fig. 8. The geometry parameters and the boundaries are quite similar as those of roughness. The cavitation is h in depth, w in width and D in interval between each. Here we only consider the homogeneously charged cases at $\psi_s = -50$ mV.

Fig. 9 shows the relationship between the flow rate and the cavitations depth when w equals $H/4$ and D equals $7H/4$. The other parameters are $c_\infty = 10^{-4}$ M and $E = 5 \times 10^2$ V/m. The relative depth h/H changes from 0 (smooth channel) to 0.3. When the cavitations are very shallow ($h < 3\%H$), the flow rate almost keep unchanged with the cavitations depth. With the cavitation depth increasing, the electrically-driven flow rate decrease sharply. If the cavitations are deep enough (such as $h > 10\%H$), the flow rate decrease becomes slow

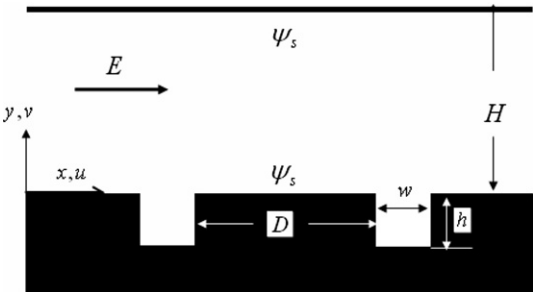

Fig. 8. Geometries and boundary conditions for the microchannel with cavitations.

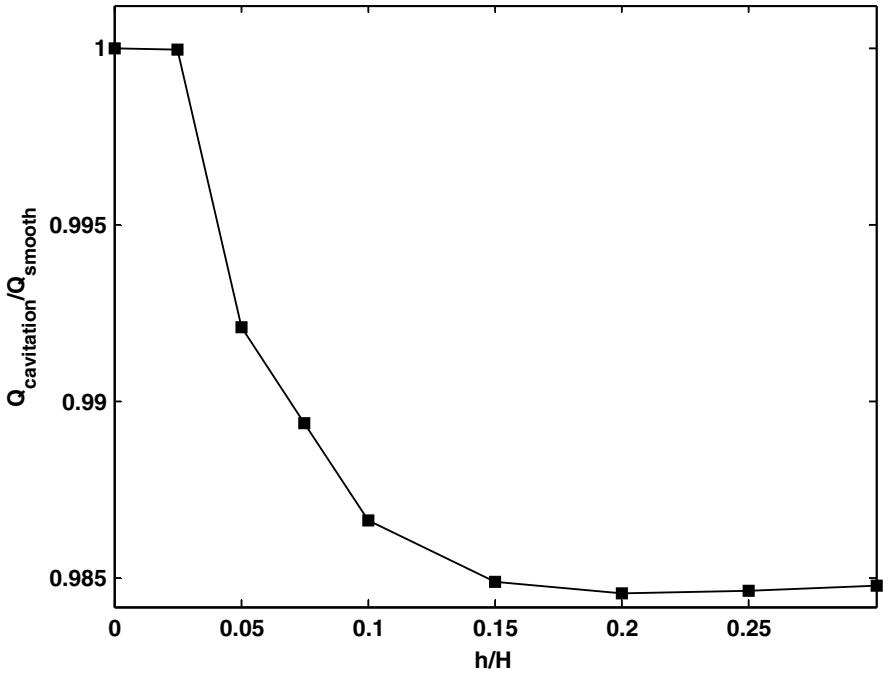

Fig. 9. Flow rate variation with the cavitations depth at $w = H/4$ and $D = 7H/4$ where $c_\infty = 10^{-4}$ M, $E = 5 \times 10^2$ V/m, $\psi_s = -50$ mV, $H = 0.4$ μm.

and the flow rate shows to be asymptote-like stable to a constant when the cavitations are very deep ($h \gg 20\%H$). Fig. 9 indicates that the cavitations effect on the flow rate is not as significant as the roughness. The electrically-driven flow rate difference in between a smooth channel and a cavitational channel is less than

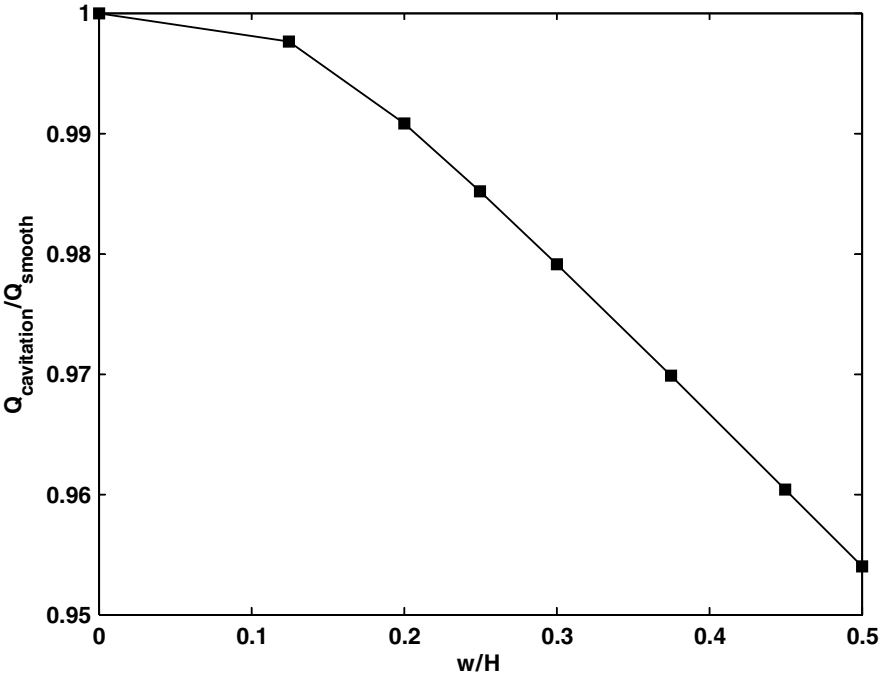

Fig. 10. Flow rate variation with the cavitations width for $c_\infty = 10^{-4}$ M, $E = 5 \times 10^2$ V/m, $\psi_s = -50$ mV, $H = 0.4$ μm.

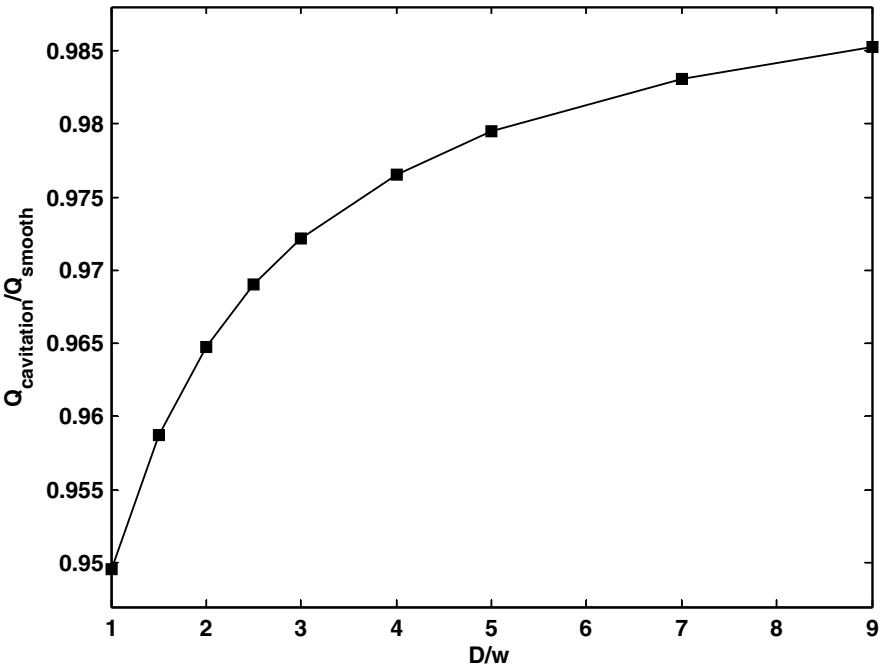

Fig. 11. Flow rate variation with the cavitations intervals for $c_\infty = 10^{-4}$ M, $E = 5 \times 10^2$ V/m, $\psi_s = -50$ mV, $H = 0.4$ μm.

3% for the current situations. The cavitations decrease the flow rate in the electro-osmotic channel flows, which is different from the reported results in previous pressure driven flows [51], however, is consistent with the atomistic simulation results very recently [53]. The reason may lie in that the cavitations decrease the electric driving force more than they decrease the surface resistance for electro-osmotic flows.

The cavitations width and interval effects on the flow rate are shown in Figs. 10 and 11. In Fig. 10, the cavitations are deep enough, $h = 0.3H$, to eliminate the depth effect on the flow rate and the cavitations interval $D = 7H/4$. The results in Fig. 10 indicate the flow rate decreases with the cavitations width. In Fig. 11, both the cavitations width and depth are fixed at $H/4$, and the interval space changes from one width to nine width. The results indicate that the sparser the cavitations are, the larger the flow rates are and closer the flow rate is to the value of a smooth channel. Comparing Fig. 11 with Fig. 6 shows the cavitations effect on the flow rate is much smaller than the roughness effect.

4. Conclusions

The Lattice Poisson–Boltzmann method, which combines two lattice evolution methods solving the nonlinear Poisson equation for electric potential distribution and solving the Navier–Stokes equations for fluid flow, were used to simulate the electro-osmotic flows in rough microchannels. The boundary conditions were correctly treated for consistency between both. The roughness and cavitations effects on the flow behaviors were therefore analyzed with various shapes and arrangements.

For electro-osmotic flows in homogeneously charged rough channels, the flow rate does not vary with the roughness height or the interval space monotonically. The flow rate varies slightly with the roughness height when the roughness is very small, and then decreases if the roughness height is greater than 5% of the channel width. The flow rate decreases first and then increase with the roughness interval space. An interval space at twice roughness width makes the flow rate minimum. For the heterogeneously charged rough channel, the flow rate increases with the roughness surface potential at a superlinear rate. For the electro-osmotic flows in cavitational microchannels, the flow rate almost does not change with the cavitations depth when the depth value is very low and decreases sharply when the depth is greater than 3% the channel width. The flow rate trends to be a constant when the cavitations are very deep. The flow rate decreases with the cavitations width while increases with the cavitations interval. The sparser the cavitations are, the closer the flow rate is to that for the smooth channel case. Since some interesting and anomalous flow behaviors predicted in this contribution have not been reported and validated, we will analyze the flow mechanism further using multi-scale simulation in the future.

Since the electro-osmotic flows in microchannels have many promising applications in microsystems, the analyzed methods and simulation results presented here provide valuable information for the design and optimization of MEMS/NEMS.

Acknowledgment

The present work is supported by the US NSF-0613085.

References

[1] K.A. Sharp, B. Honig, Electrostatic interactions in macromolecules: theory and applications, Annu. Rev. Biophys. Biophys. Chem. 19 (1990) 301–332.
[2] H.A. Stone, A.D. Stroock, A. Ajdari, Engineering flows in small devices: microfluidics toward a lab-on-a-chip, Annu. Rev. Fluid Mech. 36 (2004) 381–411.
[3] P.K. Wong, J.T. Wang, J.H. Deval, C.M. Ho, Electrokinetic in micro devices for biotechnology applications, IEEE/ASME Trans. Mechatron. 9 (2004) 366–376.
[4] D. Reyes, D. Iossifidis, P. Auroux, A. Manz, Micro total analysis systems. 1. Introduction, theory, and technology, Anal. Chem. 74 (2002) 2623–2636.
[5] H. Darguji, P.D. Yang, A. Majumdar, Ion transport in nanofluidic channels, Nano Lett. 4 (2004) 137–142.
[6] R. Karnik, R. Fan, M. Yue, D.Y. Li, P.D. Yang, A. Majumdar, Electrostatic control of ions and molecules in nanofluidic transistors, Nano Lett. 5 (5) (2005) 943–948.

[7] Q.S. Pu, S.R. Liu, Microfabricated electroosmotic pump for capillary-based sequential injection analysis, Anal. Chim. Acta. 511 (2004) 105–112.
[8] M.Z. Bazant, T.M. Squires, Induced-charge electrokinetic phenomena: theory and microfluidic applications, Phys. Rev. Lett. 92 (2004) 066101.
[9] S.M. Shin, I.S. Kang, Y.K. Cho, Mixing enhancement by using electrokinetic instability under time-periodic electric field, J. Micromech. Microeng. 15 (2005) 455–462.
[10] B. Honig, A. Nicholls, Classical electrostatics in biology and chemistry, Science 268 (5214) (1995) 1144–1149.
[11] C. Yang, D.Q. Li, Analysis of electrokinetic effects on liquid flow in rectangular microcahnnels, Colloids Surf. A 143 (1998) 339–353.
[12] D.Q. Li, Electro-viscous effects on pressure-driven liquid flow in microchannels, Colloids Surf. A 195 (2001) 35–57.
[13] D.Q. Li, Electrokinetics in Microfluidics, Academic, Oxford, 2004.
[14] J. Lee, Y. Hu, D.Q. Li, Electrokinetic concentration gradient generation using a converging–diverging microchannel, Anal. Chem. Acta 543 (2005) 99–108.
[15] C. Ye, D. Li, 3-D transient electrophoretic motion of a spherical particle in a T-shaped rectangular microchannel, J. Colloid Interf. Sci. 272 (2004) 480–488.
[16] Y.D. Hu, C. Werner, D.Q. Li, Electrokinetic transport through rough microchannels, Anal. Chem. 75 (2003) 5747–5758.
[17] Y.D. Hu, C. Werner, D.Q. Li, Influence of the three-dimensional heterogeneous roughness on electrokinetic transport in microchannels, J. Colloid Interf. Sci. 280 (2004) 527–536.
[18] D. Hlushkou, D. Kandhai, U. Tallarek, Coupled lattice-Boltzmann and finite-difference simulation of electroosmosis in microfluidic channels, Int. J. Numer. Methods Fluids 46 (5) (2004) 507–532.
[19] J.H. Masliyah, S. Bhattacharjee, Electrokinetic and Colloid Transport Phenomena, John Wiley & Sons, 2006.
[20] B. Li, D.Y. Kwok, Electrokinetic microfluidic phenomena by a lattice Boltzmann model using a modified Poisson–Boltzmann equation with an excluded volume effect, J. Chem. Phys. 120 (2004) 947–953.
[21] F.Z. Tian, B.M. Li, D.Y. Kwok, Lattice Boltzmann simulation of electroosmotic flows in micro- and nanochannels, in: International Conference on MEMS, NANO and Smart Systems (ICMENS) of 2004, Banff, Alberta, Canada, 2004, pp. 294–299.
[22] S. Melchionna, S. Succi, Electrorheology in nanopores via lattice Boltzmann simulation, J. Chem. Phys. 120 (2004) 4492–4497.
[23] Z.L. Guo, T.S. Zhao, Y. Shi, A lattice Boltzmann algorithm for electro-osmotic flows in microfluidic devices, J. Chem. Phys. 112 (14) (2005) 144907.
[24] J.K. Wang, M. Wang, Z.X. Li, Lattice Poisson–Boltzmann simulations of electro-osmotic flows in microchannels, J. Colloids Interf. Sci. 296 (2) (2006) 729–736.
[25] M. Wang, J.K. Wang, Z.X. Li, Lattice Poisson–Boltzmann simulations of electro-osmotic flows in microchannels (vol 296, pg 729, 2006), J. Colloids Interf. Sci. 300 (1) (2006) 446.
[26] J.K. Wang, M. Wang, Z.X. Li, Lattice Boltzmann simulations of mixing enhancement by the electro-osmotic flow in microchannels, Modern Phys. Lett. B 19 (28–29) (2005) 1515 SI–1518 SI.
[27] R. Qiao, N.R. Aluru, Ion concentrations and velocity profiles in nanochannel electroosmotic flows, J. Chem. Phys. 118 (10) (2003) 4692–4701.
[28] M. Wang, J. Liu, S.Y. Chen, Similarity of Electro-osmotic flows in nanochannels, Mol. Simul. 33 (3) (2007) 239–244.
[29] A.P. Thompson, Nonequilibrium molecular dynamics simulation of electro-osmotic flow in a charged nanopore, J. Chem. Phys. 119 (14) (2003) 7503–7511.
[30] D. Sundholm, Universal method for computation of electrostatic potentials, J. Chem. Phys. 122 (19) (2005) 194107.
[31] J. Shen, Efficient spectral-Galerkin method II. Direct solvers of second and fourth order equations by using Chebyshev polynomials, SIAM J. Sci. Comput. 16 (1) (1995) 74–87.
[32] J. Wu, V. Srinivasan, J. Xu, C.Y. Wang, Newton–Krylov-multigrid algorithms for battery simulation, J. Electrochem. Soc. 149 (10) (2002) A1342–A1348.
[33] P.B. Warren, Electroviscous transport problems via lattice-Boltzmann, Int. J. Modern Phys. C 8 (4) (1997) 889–898.
[34] X.Y. He, N. Li, Lattice Boltzmann simulation of electrochemical systems, Comput. Phys. Commun. 129 (2000) 158–166.
[35] J. Horbach, D. Frenkel, Lattice-Boltzmann method for the simulation of transport phenomena in charged colloids, Phys. Rev. E 64 (2001) 061507.
[36] M. Hirabayashi, Y. Chen, H. Ohashi, The lattice BGK model for the Poisson equation, JSME Int. J. Ser. B 44 (1) (2001) 45–52.
[37] M. Hirabayashi, Y. Chen, H. Ohashi, The lattice BGK solution of the QKPZ equation: Universality and scaling in fluid invasion of porous media, Transactions of JSCES, Paper-20000004, 2000.
[38] J.K. Wang, M. Wang, Z.X. Li, Lattice evolution solution for the nonlinear Poisson–Boltzmann equation in confined domains, Commun. Nonlinear Sci. Numer. Simul., in press.: doi:10.1016/j.cnsns.2006.06.002.
[39] S. Chen, G.D. Doolen, Lattice Boltzmann method for fluid flows, Annu. Rev. Fluid Mech. 30 (1998) 329–364.
[40] X.Y. He, L.S. Luo, Theory of the lattice Boltzmann method: From the Boltzmann equation to the lattice Boltzmann equation, Phys. Rev. E 56 (6) (1997) 6811–6817.
[41] Y.H. Qian, D. Dhumieres, P. Lallemand, Lattice BGK models for Navier–Stokes equation, Europhys. Lett. 17 (6BIS) (1992) 479–484.
[42] X.Y. He, S. Chen, G. Doolen, A novel thermal model for the lattice Boltzmann method in incompressible limit, J. Comput. Phys 42 (146) (1998) 282–300.
[43] Z.L. Guo, C.G. Zheng, B.C. Shi, Discrete lattice effects on the forcing term in the lattice Boltzmann method, Phys. Rev. E 65 (4) (2002) 046308.
[44] A. D'Orazio, S. Succi, Simulating two-dimensional thermal channel flows by means of a lattice Boltzmann method with new boundary conditions, Future Gen. Comput. Syst. 20 (6) (2004) 935–944.

[45] D.R. Noble, S.Y. Chen, J.G. Georgiadis, R.O. Buckius, A consistent hydrodynamics boundary condition for the lattice Boltzmann method, Phys. Fluids 7 (1) (1995) 203–209.
[46] M. Rohde, D. Kandhai, J.J. Derksen, H.E.A. Van den Akker, Improved bounce-back methods for no-slip walls in lattice-Boltzmann schemes: theory and simulations, Phys. Rev. E 67 (6) (2003) 066703.
[47] T. Inamuro, M. Yoshino, F. Ogino, A non-slip boundary condition for lattice Boltzmann simulations, Phys. Fluids 7 (12) (1995) 2928–2930, Erratum. Phys. Fluids 8(4) (1996) 1124.
[48] D. Sinton, D.Q. Li, Electroosmotic velocity profiles in microchannels, Colloids Surf. A 222 (2003) 273–283.
[49] S.T. Cui, H.D. Cochran, Electroosmotic flow in nanoscale parallel-plate channels: molecular simulation study and comparison with classical Poisson–Boltzmann theory, Mol. Simul. 30 (5) (2004) 259–266.
[50] W. Zhu, S.J. Singer, Z. Zheng, et al., Electro-osmotic flow of a model electrolyte, Phys. Rev. E 71 (4) (2005) 041501.
[51] Z.Y. Guo, Z.X. Li, Size effect on microscale single-phase flow and heat transfer, Int J. Heat Mass Transfer 46 (1) (2003) 149–159.
[52] Z.X. Li, Z.Y. Guo, Some flow and thermal phenomena at microscale, keynote, in: 1st International Conference on Microchannels and Minichannels, Rochester, NY, USA, 2003, pp. 77–92.
[53] R. Qiao, Effects of molecular level surface roughness on electroosmotic flow, Microfluid. Nanofluid. 3 (2007) 33–38.